Silicon Photonics FMCW LiDAR Chip With a Slow-Light Grating Beam Scanner

Toshihiko Baba , *Fellow, IEEE*, Takemasa Tamanuki, Hiroyuki Ito , Mikiya Kamata , Ryo Tetsuya, Saneyuki Suyama, Hiroshi Abe, and Ryo Kurahashi

(Invited Paper)

Abstract—Photonic crystal slow-light gratings fabricated using Si photonics enable high-speed, high-resolution, and wide field-of-view two-dimensional beam scanning via the thermo-optic effect. In this paper, we built a frequency-modulated continuous-wave light detection and ranging system on a chip by combining a beam scanner with Ge photodiodes for delay homodyne coherent detection. Emitting and scanning frequency-swept laser beam, point cloud images of $154 \times 32 = 4928$ points were obtained. The real-time operation and velocity imaging were also demonstrated. This device is expected to detect Lambertian targets over long distances in the 100-m class by reasonably reducing chip and optics losses and suppressing internal noise components.

Index Terms—Beam scanner, frequency-modulated continuous-wave (FMCW), light detection and ranging (LiDAR), photonic crystal, Si photonics, slow-light.

I. INTRODUCTION

LIGHT detection and ranging (LiDAR) systems, which are three-dimensional (3D) imaging sensors, have attracted great attention in conjunction with autonomous vehicles [1]. In general, LiDAR systems for long and medium ranges use a mechanical beam scanner to send a high-density optical beam to target objects. In recent years, it has been actively researched to replace mechanical scanners with nonmechanical solid-state ones to make LiDAR systems more compact, fast, flexible, and stable. For example, optical phased arrays (OPAs) [2]–[8] and focal plane arrays (FPAs) [9]–[11] have been fabricated and demonstrated using a Si-photonics platform. As an alternative

approach, we have developed a slow-light grating (SLG) beam scanner based on photonic crystal waveguides, which can also be fabricated using Si photonics [12]. It is a waveguide grating that emits the guided mode as a free-space beam and steers it with wavelength changes and/or waveguide refractive index changes. Different from usual waveguide gratings, the beam angle of the SLG is much more sensitive to the wavelength and refractive index, due to the slow-light effect. In comparison with OPA and FPA, SLG alleviates the burden of large-scale integration and phase calibration of optical antennas while enabling wide-range and high-resolution beam scanning via the thermo-optic (TO) effect for a fixed laser wavelength. We have demonstrated two-dimensional (2D) beam scanning with $40° \times 8.8°$ range, $\sim0.1°$ beam divergence [13], and 2.7-μs beam switching time [14].

As for range, the popular time-of-flight (TOF) method is difficult to apply on Si devices because 40–50 dBm order intense optical pulses used in this method produce the two-photon absorption in Si even at transparent wavelengths $\lambda > 1.5$ μm and saturate the transmission (Tx) power. As a result, the frequency-modulated continuous-wave (FMCW) method is frequently used [6], [11], [15]–[19]. In FMCW LiDARs, frequency-swept laser light is transmitted to nearby objects, and reflected light is received (Rx) in the same device and mixed with internal reference light (Ref) to produce a beat frequency via delayed homodyne detection, which provides range information. Since the Tx power must be suppressed below the eye-safe level of 10 dBm in this wavelength range, the two-photon absorption that occurs severely at >20 dBm in Si devices [20] is not considered to be a problem, even though the account of internal losses of the device is added to the launched power. Aside from low noise and high sensitivity, FMCW has negligible crosstalk with ambient light from the sun, city lighting, other LiDARs, and so on, which is a significant advantage for stable LiDAR use in complex environments. Furthermore, FMCW can detect velocity and vibration based on the Doppler shift of the beat frequency, which also provides motion information [21].

Visualizing the distance and motion of target objects enables various applications as illustrated in Fig. 1. TOF LiDARs are already used in high-end smartphones and tablets for short-range applications such as identification, capture, and surveying. They are also beginning to be implemented in autonomous vehicles, drones, and robots. The data acquired by these mobiles are accumulated for mapping and environmental monitoring.
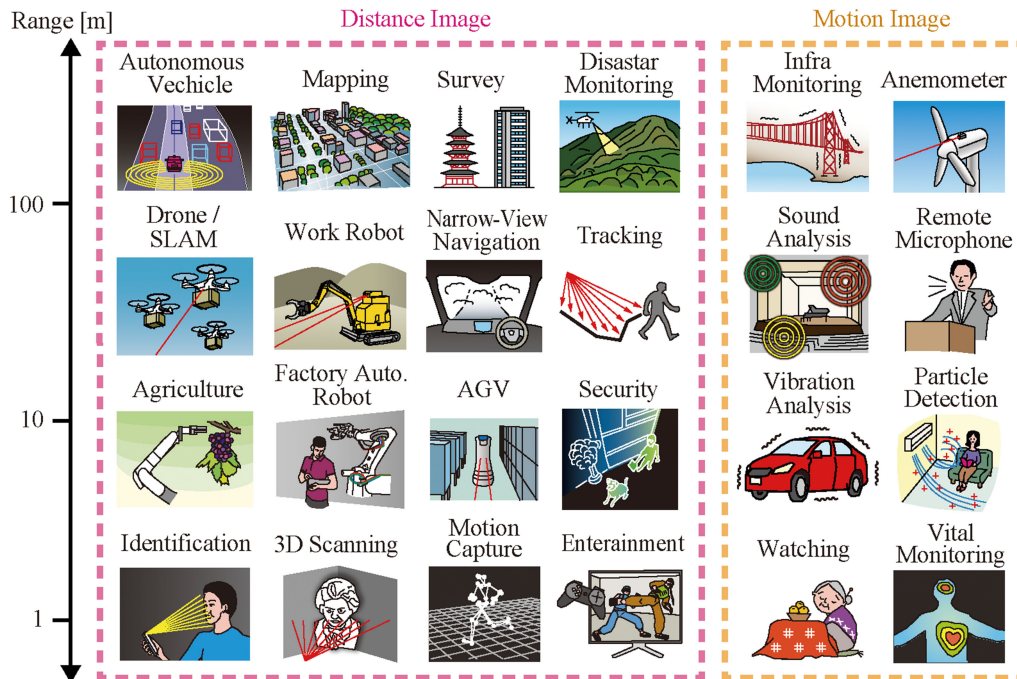
Fig. 1. Applications of FMCW LiDAR. SLM, simultaneous localization and mapping; AGV, automatic guided vehicle.

Narrow-view navigation in foggy weather is possible by extracting the forward image of the desired distance range from the entire 3D information. Security sensing can track moving objects thanks to flexible nonmechanical beam scanning that is unaffected by inertia. FMCW LiDARs can be used for all of these purposes as well. FMCW's Doppler shift measurements add additional capabilities to LiDAR, including infrastructure monitoring, sound, vibration, and airflow analysis, and watching and vital monitoring of people.

These advantages become effective when FMCW LiDARs can be manufactured as easily as TOF LiDARs using a photonic integration platform such as Si photonics. OPAs and FPAs in combination with the FMCW optical setup have been reported, showing point cloud images with hundreds of resolution points [6], [11]. In the present study, we created an FMCW LiDAR chip that combined the SLG beam scanner with other required components, resulting in point cloud images with thousands of resolution points. This paper describes the details and discusses the prospects for improving the signal-to-noise ratio (S/N) of range signals for detection of targets greater than 100 m.

II. DEVICE

The device details and fabrication process were similar to those in Refs. [12], [13], but with some changes and component additions, which are denoted as (C) and (A) in the following. Fig. 2 shows the top view of the LiDAR chip and its schematic. The chip was fabricated on a 200-mm-diameter silicon-on-insulator using a Si-photonics complementary metal-oxide-semiconductor process, whose feature size was 110 nm. The thickness of the Si layer was 205–210 nm, lower SiO_2 BOX layer 2 μm, and the SiO_2 over-cladding $\sim$2 μm. The chip included a Si-inverse-tapered spot-size converter (SSC)

endfire fiber coupler, a TO symmetric Mach-Zehnder (MZ) on/off switch (SW) (A), a homodyne detection circuit (A) with Ge balanced photodiodes (BPD) (A), left/right TO MZ SW, a couple of TO MZ SW trees, and p-i-p TO heater-loaded 32 SLGs, all of which were connected by Si wire waveguides and electrically controlled by external circuits through Al wires and bonding pads. All the components except for the pads were cladded with SiO_2. The total chip size was 9.1 $\times$ 5.5 mm^2 (C), which was mainly constrained by the size and pitch of 126 bonding pads; it would be reduced to 5 $\times$ 5 mm^2 if smaller and denser pads were available.

For low-loss optical wirings, Si singlemode waveguides of 400-nm width and Si quasi-singlemode waveguides with 3-μm width (C) were mixed through 50-μm-long adiabatic tapers. Their propagation losses were measured using a test element group (TEG) chip and transverse-electric (TE) polarized laser light to be 3.6 dB/cm and 0.2 dB/cm, respectively (in the following, the value for each component was measured similarly). The TO MZ SW had a TiN heater whose thickness, width, length, and location were 120 nm, 3 μm, 150 μm, and 1.2 μm above the Si layer, respectively. The heating power for π-phase shift was 14 mW, and the rise and fall time constant was 9–10 μs. As shown in Fig. 2(c), a tapered transition structure [22] was used for the optical coupling from the wire waveguide into the SLG, for which the modal transition loss was calculated using 3D finite-difference time-domain simulation to be 0.28 dB (theoretical values for other components were obtained similarly) and measured to be 0.6 dB.

The SLG consisted of a 1.5-mm-long (C) lattice-shifted photonic crystal waveguide (LSPCW) with a shallow grating. The hole diameter and pitch of triangular lattice photonic crystal claddings sandwiching the single line-defect waveguide channel were targeted at 192 and 394 nm, respectively, and the third-row
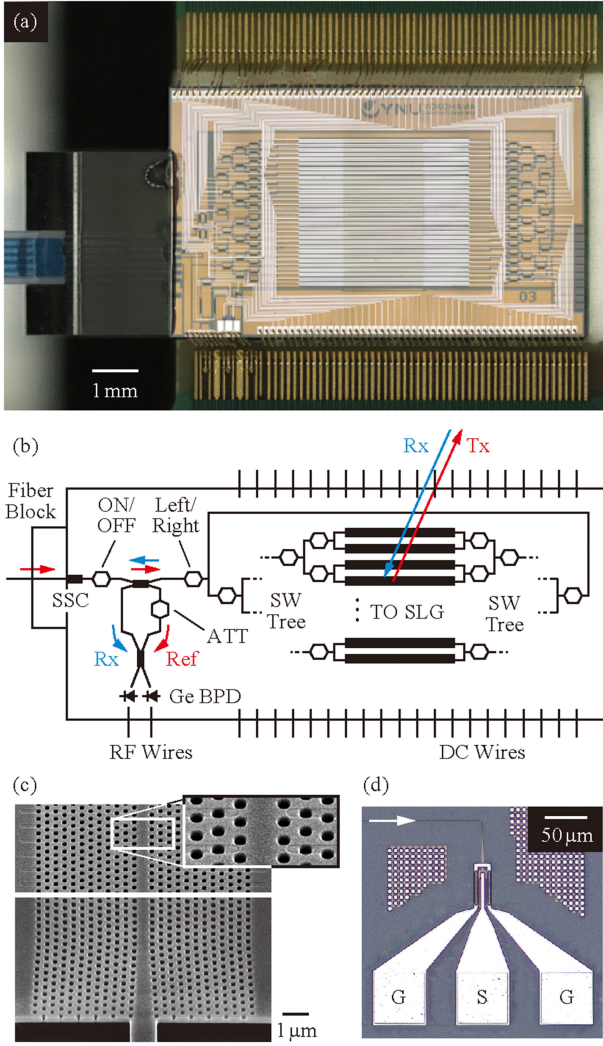
Fig. 2. Fabricated and assembled LiDAR chip of 9.1 mm × 5.5 mm size. (a) Fabricated chip bonded on Al base. (b) Schematic. (c) Scanning electron micrograph of photonic crystal waveguide obtained after removing SiO_2 over-cladding. Upper shows SLG, and lower shows the tapered transition structure without grating. (d) Ge photodiode in a TEG chip.

lattice shift was 100 nm. The group index and working spectral width of slow light with higher-order dispersion suppressed were 18–22 and 23 nm, respectively. With a grating, the slow-light mode of the SLG is radiated gradually to the out-of-plane direction to form a fan beam with the angle θ (taken from normal to the device surface) and the divergence (full-width at half maximum) $\delta\theta$ along the LSPCW and the divergence $\delta\phi$ across the LSPCW. The grating was created by first etching the Si layer shallowly and then etching the photonic crystal holes perforated. The grating's corrugation width and depth were both set at 200 and 8 ± 2.5 nm, respectively (C). The corrugations were aligned so that they overlapped with the photonic crystal's even number of rows of holes and they did not form at the waveguide channel, as shown in Fig. 2(c). This structure theoretically gives an upward emission efficiency of ~60% independently of the direction of light propagation and a radiation coefficient of ~100 dB/cm (corresponding $\delta\theta = 0.08°$) at $\lambda = 1550$ nm. The experimental

$\delta\theta$ distribution is in the range of 0.08°–0.18°, which might be affected by nonuniformities in the shallow etching.

Each SLG was equipped with a TO heater for beam scanning, which was formed by p-i-p doping into the LSPCW. The p-dopant (boron) was ion-implanted into the Si layer with a surface density of 2.0×10^{13} cm^{-2}, and the width of the i-region overlapping with the waveguide channel was set at 1.6 μm to suppress the free-carrier absorption loss. The heating current rose at a voltage V of 7 V, mainly applied to the i-region, and flew across the waveguide channel with a slope resistance of 290 Ω. For $V = 7$–32 V, the current and heating power varied in the range of 0–87 mA and 0–2.7 W (rated power), respectively, and the beam was scanned by $\Delta\theta = 25.2°$ at maximum from $\theta = 7.0°$–32.2°. By switching the direction of light propagation in the LSPCW and converting the beam angle by a prism lens [12] optimized for these θ, $\Delta\theta$ could be doubled up to >50°, although only a single direction was used in this experiment. In another preliminary experiment, an increase in $\delta\theta$ heating was observed. This was caused by temperature nonuniformity near the SLG's edges, which caused the beam angle to be slightly disturbed. We did not form the grating in this LiDAR chip within 100 μm of both edges, so the increase in $\delta\theta$ was suppressed.

The delay homodyne detection circuit employed a 2×2 coupler for dividing input light to Tx and Ref and for guiding half of Rx light to the subsequent 2×2 couplers to mix with Ref and detect in the Ge BPD, as shown in Fig. 2(d). Since the on-chip circulator is not available, the first 2×2 coupler caused an essential 3 dB loss for both Tx and Rx. A TO MZ attenuator (ATT) was used in the reference path to moderately reduce the Ref power so that the responsivity of Ge BPD was not saturated. The Ge BPD was selectively grown on a p-doped Si open window with a thin SiO_2 cover. The top of the Ge was n-doped (phosphorus) and then annealed to remove defects and activate the dopants. The responsivity and dark current at zero bias were 0.7–1.0 A/W at $\lambda = 1.50$–1.58 μm and <10 nW, respectively. The responsivity did not increase for bias voltages from -1 to -3 V, whereas the dark current increased to as high as 4–250 μA. Therefore, we used the BPDs under zero bias.

After dicing the wafer and polishing the chip facet, the chip was die-bonded on an Al base and wire-bonded to the surrounding printed circuit board, as shown in Fig. 3(a). Polarization-maintaining core-shrunk single-mode fiber was directly attached to the SSC with UV resin.

III. LiDAR Operation

Fig. 3(b) shows the schematic of the measurement setup. TE-polarized continuous-wave laser light ($\lambda = 1539$ nm) from a bench-top tunable laser source (Santec TSL-550) was input into the $LiNbO_3$ in-phase/quadrature-phase (I–Q) modulator (Thorlabs LN86-14) to produce frequency-modulated light via the single sideband (SSB) modulation condition, where saw-tooth frequency-swept signals with a modulation bandwidth $B = 10$ GHz and sweep period $T = 100$ μs were produced using an arbitrary waveform generator (Keysight M8195A). We con-firmed that, when compared to double sideband signals, the SSB signal improved the signal-to-noise ratio (S/N) and suppressed
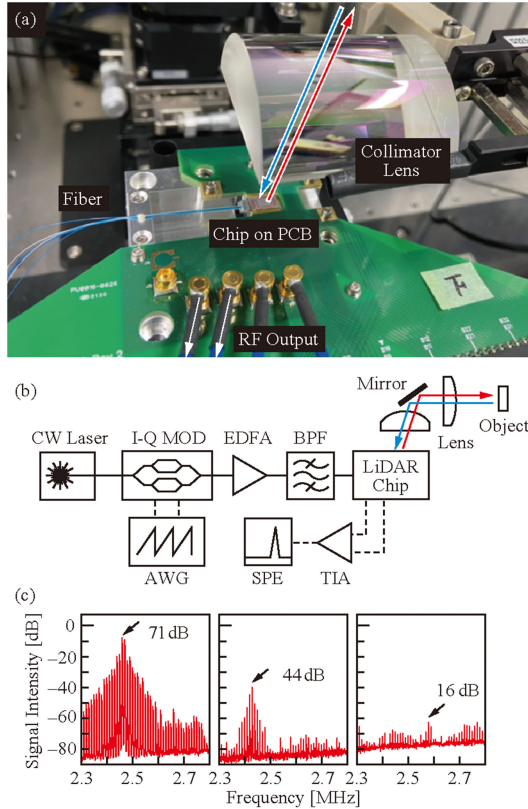
Fig. 3.   FMCW LiDAR setup. (a) Appearance and (b) schematic. (c) Observed beat spectrum for the mirror (left), retroreflective sheet (middle), and plaster (right) as a target.

Fig. 4.   Point cloud images of a tilted board covered with a retroreflective sheet. (a) Intensity profile. (b) Range profile of $154 \times 32 = 4928$ points.

the fluctuation in the beat spectrum [23]. The light from the fiber was input to the chip after being amplified by an erbium-doped fiber amplifier and a band-pass filter (the power launched to the chip was approximately 5 dBm). The fan beam radiated from the SLG was collimated in the ϕ direction by a plano-convex lens with a focal length $f = 50.8$ mm. In the first experiment, another lens of $f = 700$ mm was also inserted 300-mm away from the chip to reduce the small divergence $\delta\theta$ to approximately half. The insertion loss from the fiber to the beam was 15 dB, and therefore, the Tx power was -7 dBm. The beat signal detected by Ge BPD between the Rx and power-optimized Ref light was analyzed by a spectrum analyzer (SPE, Rohde & Schwarz FSW43) after amplification by a differential trans-impedance amplifier (TIA). Fig. 3(c) displays an example beat spectrum for a mirror as a target. The maximum S/N was 71 dB at a distance $L = 3.9$ m.

In the LiDAR operation, we removed the second lens and targeted such short distances in the laboratory room. We scanned the beam in the range of $5.1° \times 2.8°$ with $154 \times 32 = 4928$ points, recorded the peak intensity and frequency of the beat spectrum, and constructed the point cloud images. Controlling the SW trees and SLGs was used to scan the optical beam. The average power consumption for the eight TO heaters in the SWs and ATT was less than 60 mW. The p-i-p heater of the SLG was operated with a voltage range of 7.5–20 V. The corresponding power range was 0.2–1.4 W, and the average power consumption was 0.8 W. For the same voltage, the beam angle θ slightly differed between SLGs because of some nonuniformities. These

TiN and p-i-p heaters were driven and calibrated by op-amps with digital-analog converters controlled by a personal computer through an analog discovery 2 (Digilent) as a universal serial bus and serial peripheral interface converter. The SPE was also controlled by the personal computer via the general path interface bus. Furthermore, it acquired each frequency in the SPE using the peak search mode, calculated the range, and plotted the point cloud image. This series of processes from the beam scanning to the image acquisition was synchronized and automatically operated by a Python program. Although S/N = 71 dB was observed for the mirror, the value fluctuated between different beam angles. S/N was reduced to 16 dB when the target was changed to a plaster as an approximate Lambertian scatterer, as shown in Fig. 3(c). For the mirror, the efficiency η of returned light captured by the reception aperture A of the device is expressed as $\eta = 10 \log_{10}[A/\pi(L\delta\theta)^2]$ [dB]. For $\delta\theta = 0.1°$, $L = 3.9$ m and $A = 3.47$ mm^2, which was estimated from SLG's effective radiation length, ϕ-directional divergence, and lens aperture, $\eta = -16.2$ dB. For a Lambertian scatterer, which is considered as a standard target for LiDARs, $\eta = 10 \log_{10}(A/\pi L^2)$ [dB] $= -71.4$ dB under the same condition. Taking into account the linear relationship between the received signal power and the beat signal intensity in coherent detection, this comparison shows that Lambertian scatter reduces the S/N by 55.2 dB, which explains the measured S/N well. To compensate for the severe reduction in S/N, we covered target objects with a retroreflective sheet (OEALITE AP1000), which improved the S/N to 44 dB.

Fig. 4(a) and (b) shows the point cloud images of the signal intensity and range acquired for a tilted flat board. The intensity
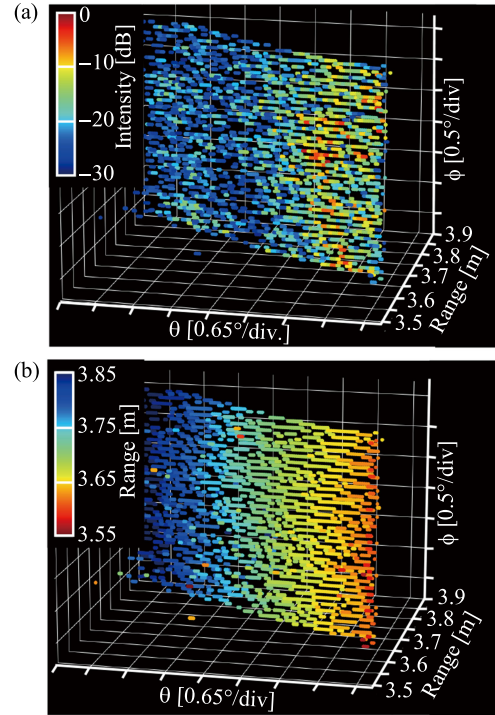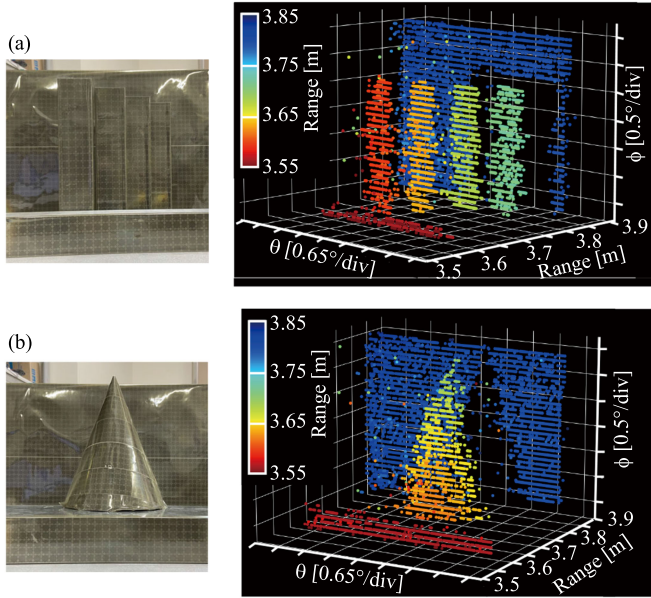
Fig. 5. Point cloud images of a tilted board covered with a retroreflective sheet. (a) Intensity profile. (b) Range profile of $154 \times 32 = 4928$ points.
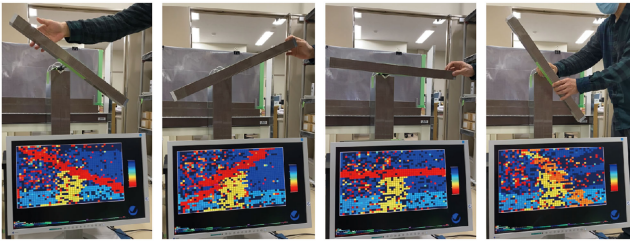

Fig. 6. Realtime operation of LiDAR chip. Range profile of rotating bar of $50 \times 32 = 1600$ points is displayed as a color tile image, where color shows the distance from 3.10 to 3.95 m.
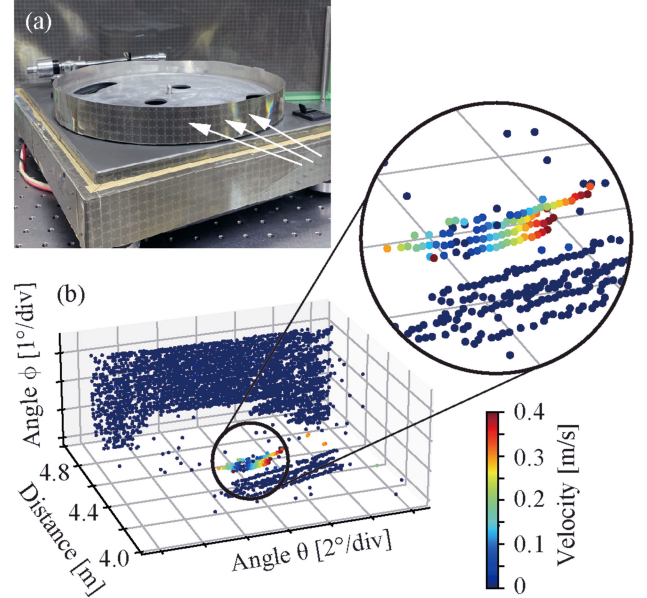

Fig. 7. Distance and velocity imaging of rotating turntable. (a) Appearance of turntable covered with retroreflective sheet. (b) Point cloud image where color depict the velocity in the direction along the irradiated beam.

on the left side decreased due to an increase in the lens's collimation error rather than an increase in distance. As previously reported [21], a prism lens can be used to compensate for this error. In Fig. 4(b), the distance of the board shifted in steps of 15 mm, which was the resolution of the range determined by the frequency sweep bandwidth $B = 10$ GHz. Fig. 5(a) and (b) shows the point cloud range images of stepwise rectangular rods and cones, respectively, for which we confirmed 3D profiles. The rod edges can be further smoothed by calibrating θ for different ϕ. Fig. 6 demonstrates a real-time acquisition of $50 \times 32 = 1600$ points. In this experiment, field-programmable gate arrays (FPGA, Xilinx XC7A35T, XC7K325T, and XC7Z020) were used to perform scan control, spectral analysis, and display output, respectively. The sweep period was changed to $T = 266$–96 μs to obtain a framerate of 2.3–6.5 fps, respectively. The noisy point was increased by 16-bit signal quantization in the used FPGA, which was less than SPE's 24-bit, but the rotating rectangular rod was observed. Furthermore, when the number of points was reduced to $20 \times 16 = 320$, a 32-fps operation was achieved.

Simultaneous distance and velocity imaging were also demonstrated for the turntable, as shown in Fig. 7. The measurement condition other than $T = 64$ μs was the same as in Figs. 4 and 5. Here the distance and velocity were obtained, respectively, from the center frequency and spacing of split beat spectrum caused by the Doppler shift. As displayed in the color plot, the velocity was detected only on the sidewall of the turntable except where the Tx light hit normal to the sidewall.

IV. Discussion

Now we discuss the prospect for the image acquisition of a standard Lambertian scatterer using this device. The catastrophic-optical damage power of the chip is 23 dBm, whereas the launched power was suppressed to 5 dBm. When the power was increased from this value, the noise floor of the signal spectrum increased, and the S/N degraded. This, we believe, is due to the saturation of the BPD response or the reduction of restricted intensity noise at the balanced detection caused by the contamination of locally reflected light inside or outside of the chip. As the evidence for this, we performed a test experiment of Tx/Rx separate configuration, as shown in Fig. 8. Here, the modulated light at the eye-safe power of 10 dBm was directly transmitted to a plaster rod through a simple fiber collimator, and scattered light was detected by the LiDAR chip at $L = 3.91$ m with the reference light input suppressed by a 99:1 fiber coupler in advance. The S/N of the beat signal reached 29 dB, a 13 dB improvement over the result shown in Fig. 3(c). When the Tx power was increased to 17 dBm, the S/N was increased to 36 dB. The simple increase in S/N with increasing Tx power suggests that a separate Tx/Rx configuration can suppress contamination. Furthermore, the separate configuration can help avoid the 3 dB essential loss at the first 2×2 coupler.
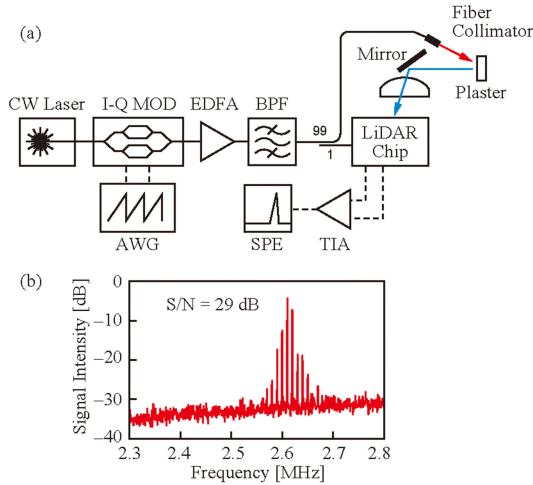
Fig. 8. Test experiment of Tx/Rx separate configuration. (a) Optical setup. (b) FMCW beat spectrum when plaster rod was used as a target and Tx beam power was set at eye-safe power of 10 dBm.

TABLE I
ESTIMATED OPTICAL LOSSES

Components	Loss	No./length	Subtotal
Fiber to SSC	~3	1	~3 dB
Wire waveguides	3.6 dB/cm 0.2 dB/cm	<0.05 cm 1.6 cm	~0.5 dB
On/off SW	0.2 dB	1	0.2 dB
2 × 2 coupler for Tx/Ref	3 + 0.1 dB	1	3.1 dB
Left/right SW	0.2 dB	1	0.2 dB
SW tree	0.2 dB	5	1.0 dB
Wire waveg./SLG transition	0.6 dB	1	0.6 dB
SLG	~1.5 dB	1	~1.5 dB
Downward radiation	2.2 dB (calc.)	1	2.2 dB
Sidelobe	1.5 dB (calc.)	1	1.5 dB
Collimator lens	~1 dB	1	~1 dB
3 dB coupler for Rx/Ref	0.1 dB	1	0.1 dB
			Total
Tx from fiber to free space beam including 2 × 2 coupler			14.8 dB
Rx from free space beam to BPD including 2 × 2 coupler			11.7 dB

Table I summarizes the optical losses estimated for the components, excluding fine Rx beam coupling condition. The Tx light suffers from 5.6 dB excess loss between the input fiber and SLG, in addition to the 3 dB essential loss. The SLG adds 5.2 dB caused by the scattering and absorption, downward radiation, and sidelobes not captured by the collimator lens. Considering a 1 dB additional loss in the lens, 14.8 dB is totally estimated for Tx. We assume that returned light is coupled into the SLG with the same loss as for Tx. Since it is finally detected by the BPD, 11.7 dB is totally estimated for Rx.

On the other hand, Table II summarizes the expected loss reduction. First, the essential loss can be neglected by separating Tx and Rx SLGs. Excess losses of other components can be reduced by optimizations and/or different configurations. The fiber coupling loss has been reduced to 0.3 dB using Si_3N_4 SSC [24]. The loss of the 1 × 2 and 2 × 2 couplers is theoretically 0.05 dB, and MZ SWs is 0.1 dB. The modified transition between the wire waveguide and SLG has been reduced to 0.21 dB experimentally

TABLE II
EXPECTED OPTICAL LOSSES FOR TX/RX SEPARATE CONFIGURATION

Components	Loss	No./length	Subtotal
Fiber to SSC	0.3	1	0.3 dB
Wire waveguides	1 dB/cm 0.2 dB/cm	<0.05 cm 1.2 cm	0.3 dB
On/off SW	0.1 dB	1	0.1 dB
Left/right SW	0.1 dB	1	0.1 dB
SW tree	0.1 dB	5	0.5 dB
Wire waveg./SLG transition	0.1 dB	1	0.1 dB
SLG	0.5 dB	1	0.5 dB
Downward radiation	0.4 dB	1	0.4 dB
Sidelobe	0.5 dB	1	0.5 dB
Collimator lens	0.5 dB	1	0.5 dB
3 dB coupler for Rx/Ref	0.05 dB	1	0.05 dB
			Total
Tx from fiber to free space beam			3.4 dB
Rx from free space beam to BPD			3.05 dB

and 0.12 dB theoretically [25]. The loss of SLG can be reduced by suppressing the p doping concentration without degrading the electrical characteristics. The downward radiation loss of 2.2 dB can also be reduced to 0.4 dB theoretically by employing a unidirectional structure SLG [26]; in this case, separate SLGs are prepared for left and right propagation. We anticipate that further grating structure optimizations will suppress the sidelobe and beam divergence, reducing collimation loss. The Tx and Rx losses then drop to as low as 3.4 and 3.05 dB, respectively (reductions of 11.4 and 8.65 dB). For this Tx loss, the light source output required becomes <14 dBm, considering the eye-safe power. This value is reasonably achievable in a current singlemode laser diode. For the reduced Rx loss, S/N for $L = 3.91$ m in Fig. 8 will be improved to >37 dB, which allows the longest detectable L to >270 m without margin and >87 m with a 10 dB margin. Further improvement will be possible by employing a serial-arrayed SLG configuration [27], in which the reception aperture is increased effectively without increasing the loss. In a four SLG array, the S/N has been improved by 12 dB, which increases the detectable distance to four times.

For the experiment of Fig. 8, the Tx power was 10 dBm, the capture efficiency η calculated was −71.4 dB, the Rx loss estimated was 11.7 dB, and the measured S/N was 29 dB. Therefore, the minimum detected signal optical power is approximately −102 dBm. If this LiDAR is assumed to be used at $L = 1$ m in the shortest case, η becomes −59.6 dB, and the detected signal optical power will be −53 dBm after the loss reduction in Table II. As a result, the dynamic range is limited to 50 dB, which prevents saturation in the TIA. The saturation of the BPD is determined not by such low signal power, but by the reference power and contaminant components, as previously stated.

V. CONCLUSION

We fabricated Si photonics full-integrated FMCW LiDAR chip incorporating SLG gratings. The acquisition of 4928 points in a point cloud image for target objects covered with retroreflective film at 3–5 m distances was made possible by non-mechanical beam scanning with a fixed wavelength laser light

and TO control of SLGs and SWs. Except for the observation of a single-pixel FMCW signal and the demonstration using a mechanical beam scanner, this is the third demonstration of such a full-integrated FMCW LiDAR chip, including the nonmechanical beam scanner, following those in Refs. [6], [11]. However, the number of pixels in the image in this study is much larger than those suggested or reported in these papers, which is attributed to the high-resolution of the SLG scanner. The real-time operation with 2.3–32 fps framerates and the velocity imaging from the Doppler shift measurement were also demonstrated. By reducing component losses and separating Tx and Rx SLGs, a practical LiDAR chip usable for Lambertian targets at a 100-m class distance will be possible. Parallel operation in the space and/or wavelength domains will enable a higher framerate while maintaining a large number of image pixels [28].

REFERENCES

[1] Y. Li and J. Ibanez-Guzman, "Lidar for autonomous driving: The principles, challenges, and trends for automotive lidar and perception systems," *IEEE Signal Process. Mag.*, vol. 37, no. 4, pp. 50–61, Apr. 2020.

[2] K. Van Acoleyen, H. Rogier, and R. Baets, "Two-dimensional optical phased array antenna on silicon-on-insulator," *Opt. Exp.*, vol. 18, no. 13, pp. 13655–13660, Jun. 2010.

[3] D. N. Hutchison *et al.*, "High-resolution aliasing-free optical beam steering," *Optica*, vol. 3, no. 8, pp. 887–890, Apr. 2016.

[4] T. Komljenovic, R. Helkey, L. Coldren, and J. E. Bowers, "Sparse aperiodic arrays for optical beam forming and LiDAR," *Opt. Exp.*, vol. 25, no. 3, pp. 2511–2528, Jan. 2017.

[5] S. W. Chung, H. Abediasl, and H. Hashemi, "A monolithically integrated large-scale optical phased array in silicon-on-insulator CMOS," *IEEE J. Solid State Circuits*, vol. 53, no. 1, pp. 275–296, Jan. 2018.

[6] C. V. Poulton *et al.*, "Long-range LiDAR and free-space data communication with high-performance optical phased arrays," *IEEE J. Sel. Top. Quantum Electron.*, vol. 25, no. 5, Sep./Oct. 2019, Art. no. 7700108.

[7] T. Kim *et al.*, "A single-chip optical phased array in a wafer-scale silicon photonics/CMOS 3D-integration platform," *IEEE J. Solid State Cir.*, vol. 54, no. 11, pp. 3061–3074, Nov. 2019.

[8] S. A. Miller *et al.*, "Large-scale optical phased array using a low-power multi-pass silicon photonic platform," *Optica*, vol. 7, no. 1, pp. 3–6, Jan. 2020.

[9] D. Inoue, T. Ichikawa, A. Kawasaki, and T. Yamashita, "Demonstration of a new optical scanner using silicon photonics integrated circuit," *Opt. Exp.*, vol. 27, no. 3, pp. 2499–2508, Feb. 2019.

[10] Y.-C. Chang *et al.*, "2D beam steerer based on metalens on silicon photonics," *Opt. Exp.*, vol. 29, no. 2, pp. 854–864, Jan. 2021.

[11] C. Rogers *et al.*, "A universal 3D imaging sensor on a silicon photonics platform," *Nature*, vol. 590, no. 7845, pp. 256–261, Feb. 2021.

[12] H. Ito *et al.*, "Wide beam steering by slow-light waveguide grating and prism lens," *Optica*, vol. 7, no. 1, pp. 47–52, Jan. 2020.

[13] T. Tamanuki, H. Ito, and T. Baba, "Thermo-optic beam scanner employing silicon photonic crystal slow-light waveguides," *J. Lightw. Technol.*, vol. 39, no. 4, pp. 904–911, Feb. 2021.

[14] J. Gondo, H. Ito, T. Tamanuki, and T. Baba, "Space-time-domain observation of high-speed optical beam scanning in a thermo-optic Si photonic crystal slow-light beam scanner," *Opt. Lett.*, vol. 46, no. 15, pp. 3600–3603, Jul. 2021.

[15] F. Aflatouni, B. Abiri, A. Rekhi, and A. Hajimiri, "Nanophotonic coherent imager," *Opt. Exp.*, vol. 23, no. 4, pp. 5117–5125, Feb. 2015.

[16] A. Martin *et al.*, "Photonic integrated circuit-based FMCW coherent LiDAR," *J. Lightw. Technol.*, vol. 36, no. 19, pp. 4640–4645, Oct. 2018.

[17] M. Okano and C. Chong, "Swept source Lidar: Simultaneous FMCW ranging and nonmechanical beam steering with a wideband swept source," *Opt. Exp.*, vol. 28, no. 16, pp. 23898–23915, Aug. 2020.

[18] J. Riemensberger *et al.*, "Massively parallel coherent laser ranging using a soliton microcomb," *Nature*, vol. 581, no. 7807, pp. 164–170, May 2020.

[19] Z. Li, Z. Zang, Y. Han, L. Wu, and H. Y. Fu, "Solid-state FMCW LiDAR with two-dimensional spectral scanning using a virtually imaged phased array," *Opt. Exp.*, vol. 29, no. 11, pp. 16547–16562, May 2021.

[20] T. Baba *et al.*, "Development of silicon photonics slow light LiDAR," *IEICE Trans. Electron.*, vol. J103-C, no. 11, pp. 434–452, 2020.

[21] S. Suyama, H. Ito, R. Kurahashi, H. Abe, and T. Baba, "Doppler velocimeter and vibrometer FMCW LiDAR with Si photonic crystal beam scanner," *Opt. Exp.*, vol. 29, no. 19, pp. 30727–30734, 2021.

[22] Y. Terada *et al.*, "Optimized optical coupling to silica-clad photonic crystal waveguide," *Opt. Lett.*, vol. 42, no. 22, pp. 4695–4698, Nov. 2017.

[23] M. Kamata, Y. Hinakura, and T. Baba, "Carrier-suppressed single sideband signal for FMCW LiDAR using Si photonic crystal optical modulators," *J. Lightw. Technol.*, vol. 38, no. 8, pp. 2315–2321, Apr. 2020.

[24] Y. Maegami *et al.*, "Simple and fully CMOS-compatible low-loss fiber coupling structure for a silicon photonics platform," *Opt. Lett.*, vol. 45, no. 7, pp. 2095–2098, Apr. 2021.

[25] R. Shiratori, M. Nakata, K. Hayashi, and T. Baba, "Particle swarm optimization of silicon photonic crystal waveguide transitions," *Opt. Lett.*, vol. 46, no. 8, pp. 1904–1907, Apr. 2021.

[26] S. Suyama, H. Ito, R. Kurahashi, H. Abe, and T. Baba, "Doppler velocimeter and vibrometer FMCW LiDAR with Si photonic crystal beam scanner," *Opt. Exp.*, vol. 29, no. 19, pp. 30727–30734, Sep. 2021.

[27] R. Tetsuya *et al.*, "Si photonic crystal optical antenna serial array and frequency-modulated continuous-wave light detection and ranging action," *Appl. Phys. Lett.*, vol. 119, no. 23, Dec. 2021, Art. no. 231103.

[28] H. Ito, T. Tatebe, H. Abe, and T. Baba, "Wavelength-division multiplexing Si photonic crystal beam steering device for high throughput parallel sensing," *Opt. Exp.*, vol. 26, no. 20, pp. 26145–26155, Sep. 2018.

Toshihiko Baba (Fellow, IEEE) received the B.E., M.E., and Ph.D. degrees from the Division of Electrical and Computer Engineering, Yokohama National University, Yokohama, Japan, in 1985, 1987, and 1990, respectively. He became an Associate Professor and a Full Professor with Yokohama National University in 1994 and 2005, respectively. He has studied ARROW waveguides, vertical cavity surface emitting lasers, microdisk lasers, photonic crystals, and Si photonics. His first demonstration includes photonic crystal waveguides and dispersion-engineered slow-light propagation, high-speed photonic crystal modulators, beam scanners, nanolasers, biosensors and LEDs, and various Si photonics passive components, including small bend, splitter, crossing, and arrayed waveguide grating. He is the author or coauthor of more than 220 journal papers. He is a Member of IEICE and JSAP, a Fellow Member of Optica, and an Associate Member of the Science Council of Japan. He was the Vice President of JSAP from 2018 to 2020. He was the recipient of JSPS Award in 2005, IEEE/LEOS Distinguished Lecturer Award in 2006/2007, Ichimura Academic Award in 2012, and Education, Culture, Sports, Science Minister's Commendation in 2016.

Takemasa Tamanuki received the B.E. degree from the Faculty of Science, Tokyo University of Science, Tokyo, Japan, in 1988, and the M.E. and Ph.D. degrees from the Graduate School, Tokyo Institute of Technology, Tokyo, Japan, in 1990 and 1993, respectively, for his study on GaAs microcavity VCSELs. Since 1993, he has been with NEC, OPTBAHN, and Ibiden USA R&D. Since 2019, he has been a R&D staff with Yokohama National University, Yokohama, Japan. He has studied and developed semiconductor lasers, telecom and datacom modules and sub-systems, and FMCW LiDAR devices.

Hiroyuki Ito received the B.E., M.E., and Ph.D. degrees from the Division of Electrical and Computer Engineering, Yokohama National University, Yokohama, Japan, in 2013, 2015, and 2019, respectively. From 2019 to 2021, he was a R&D staff with Yokohama National University and then he joined Santec Corp., in 2021. He has studied Si photonics multi or demultiplexers based on coupled microrings, WDM transmitters, including photonic crystal modulators, and slow-light FMCW LiDAR devices. He is a Member of JSAP.

Mikiya Kamata received the B.E. and M.E. degrees from the Division of Electrical and Computer Engineering, Yokohama National University, Yokohama, Japan, in 2019 and 2021, respectively. He has studied photonic crystal I/Q modulators and their application to FMCW LiDAR devices. He is a Member of JSAP.

Ryo Tetsuya received the B.E. and M.E. degrees from the Division of Electrical and Computer Engineering, Yokohama National University, Yokohama, Japan, in 2018 and 2019, respectively. He has studied a serial array configuration of photonic crystal beam scanner and its application to FMCW LiDAR devices. He is a Member of JSAP.

Hiroshi Abe received the B.E., M.E., and Ph.D. degrees from the Division of Electrical and Computer Engineering, Yokohama National University, Yokohama, Japan, in 2009, 2011, and 2016, respectively. From 2016 to 2020, he was a R&D staff with Yokohama National University and then he joined Furukawa Electric Company Ltd., in 2021. During his thesis work, he studied GaInAsP photonic crystal nanolaser array and its application to live cell imaging. He developed slow-light FMCW LiDAR devices as a R&D staff. He is a Member of JSAP.

Saneyuki Suyama received the B.E. degree from the Department of Electrical and Computer Engineering, Yokohama National University, Yokohama, China, in 2021. He has studied the detection of Doppler shift in slow-light FMCW LiDAR devices. He is a Member of JSAP.

Ryo Kurahashi received the M.E. degree from the Division of Electrical and Computer Engineering, Yokohama National University, Yokohama, Japan, in 2021. He has studied photonic crystal slow-light FMCW LiDAR devices. He is currently with NEC Corp.